Improving InSAR geodesy using global atmospheric models

Romain Jolivet[1], Piyush Shanker Agram[1,6], Nina Y. Lin[1], Mark Simons[1,2], Marie-Pierre Doin[3,4], Gilles Peltzer[5,2], Zhenhong Li[6]

Corresponding author: R. Jolivet, Seismological Laboratory, Department of Geological and Planetary Sciences, California Institute of Technology, 1200 E California Blvd, Pasadena, CA 91125-2100, USA. (rjolivet@caltech.edu)

[1]Seismological Laboratory, Department of

Abstract. Spatial and temporal variations of pressure, temperature and water vapor content in the atmosphere introduce significant confounding delays in Interferometric Synthetic Aperture Radar (InSAR) observations of ground deformation and bias estimates of regional strain rates. Producing

Geological and Planetary Sciences,
California Institute of Technology,
California 91125, USA.

[2]Jet Propulsion Laboratory, California Institute of Technology, Pasadena, California 91109, United States of America.

[3]ISTerre, Universit Grenoble Alpes, BP 53, 38041 Grenoble, France.

[4]ISTerre, CNRS, BP 53, 38041 Grenoble, France.

[5]Department of Earth and Space Science, University of California Los Angeles, United States of America.

[6]COMET+, School of Geographical and Earth Sciences, University of Glasgow, UK

[7]Now at Jet Propulsion Laboratory, NASA, California, USA.

robust estimates of tropospheric delays remains one of the key challenges in increasing the accuracy of ground deformation measurements using InSAR. Recent studies revealed the efficiency of global atmospheric reanalysis to mitigate the impact of tropospheric delays, motivating further exploration of their potential. Here, we explore the effectiveness of these models in several geographic and tectonic settings on both single interferograms and time series analysis products. Both hydrostatic and wet contributions to the phase delay are important to account for. We validate these path delay corrections by comparing with estimates of vertically integrated atmospheric water vapor content derived from the passive multi-spectral imager MERIS, onboard the ENVISAT satellite. Generally, the performance of the prediction depends on the vigor of atmospheric turbulence. We discuss (1) how separating atmospheric and orbital contributions allows one to better measure long wavelength deformation, (2) how atmospheric delays affect measurements of the surface deformation following earthquakes and (3) we show that such a method allows us to reduce biases in multi-year strain rate estimates by reducing the influence of unevenly sampled seasonal oscillations of the tropospheric delay.

1. Introduction

Synthetic Aperture Radar Interferometry (InSAR) has been successfully used to measure ground deformations related to hydrologic, volcanic and tectonic processes [e.g. *Bawden et al.*, 2001; *Beauducel et al.*, 2000; *Massonnet et al.*, 1992]. Rapid, large-amplitude deformation signals such as co-seismic displacement fields [e.g. *Simons et al.*, 2002; *Lasserre et al.*, 2005] or volcano-tectonic episodes [e.g. *Pritchard and Simons*, 2002; *Wright et al.*, 2004; *Doubre and Peltzer*, 2007; *Grandin et al.*, 2010] are now routinely measured by InSAR. Still, the detection of low amplitude, long wavelength deformation fields such as those due to interseismic strain accumulation or post-seismic motion remains challenging because of interferometric decorrelation, inaccurate orbits and atmospheric propagation delays [e.g. *Peltzer et al.*, 2001; *Wright et al.*, 2001; *Ryder et al.*, 2007; *Wen et al.*, 2012; *Jolivet et al.*, 2012; *Grandin et al.*, 2012; *Béjar-Pizarro et al.*, 2013]. Here, we focus on a specific method to mitigate the impact of atmospheric artifacts.

Spatio-temporal variations of the refractivity of air can introduce a change in the measured interferometric phase, hereafter called the Atmospheric Phase Screen (APS). This phase change, or phase delay, can be on the order of several centimeters and often overwhelms the deformation signal of interest [*Hanssen*, 2001]. These phase delays result from the combined effects of turbulent mixing in the atmosphere (hereafter called turbulent delay) and stratification of the lower troposphere (hereafter called stratified delay) [e.g. *Hanssen*, 2001; *Emardson et al.*, 2003; *Doin et al.*, 2009]. Multiple studies consider the turbulent atmospheric delay patterns as random in space and time, which can be mitigated by temporal filtering of large time series of SAR acquisitions [e.g *Ferretti et al.*,

2001; *Berardino et al.*, 2002; *Hooper et al.*, 2007; *Cavalié et al.*, 2007; *Jolivet et al.*, 2012; *Hetland et al.*, 2012]. On the other hand, stratified tropospheric delay can introduce a long term bias in estimates of strain rates when using stacking or more involved time series methods, when seasonal oscillations are not well-sampled in time [*Doin et al.*, 2009].

Proposed correction methods can be divided into two groups, the empirical and the predictive methods. Empirical methods evaluate the dependency of interferometric phase on elevation within individual interferograms [e.g. *Beauducel et al.*, 2000]. Several techniques have been developed to separate contributions from residual orbits, tectonic deformation and the stratified tropospheric signal, including the use of *a priori* information from a deformation model [e.g. *Cavalié et al.*, 2008; *Elliott et al.*, 2008] or the evaluation of a local phase-topography relationship [*Lin et al.*, 2010; *Béjar-Pizarro et al.*, 2013]. Unfortunately, empirical methods cannot be easily used when the expected deformation signal correlates with topography, such as over volcanoes [e.g. *Delacourt et al.*, 1998] or across major topographic steps [e.g. *Elliott et al.*, 2008]. Such a limitation might be overcome by decomposing the interferometric phase and associated topography over multiple spatial wavelengths to separate the different contributions before proceeding to the estimation [*Lin et al.*, 2010; *Shirzaei and Bürgmann*, 2012]. Still, the relationship between phase and topography inferred using such empirical methods depends on the spatial extent of the SAR scene, sometimes leading to wrong estimates of the spatial variations of the tropospheric stratification. Empirical approaches are successful in selected cases, but their use cannot be generalized and their performances should be carefully evaluated for each case (see Supp. Mat.).

Predictive methods are based on inputs from external meteorological datasets to compute synthetic delay maps and directly correct for tropospheric delays in interferograms. Numerous methods have been developed using local meteorological data [e.g. *Delacourt et al.*, 1998], GPS zenith delay measurements [*Williams et al.*, 1998; *Webley et al.*, 2002; *Li et al.*, 2006a; *Onn and Zebker*, 2006; *Li et al.*, 2009], satellite multi-spectral imagery [e.g. *Li et al.*, 2006b, 2012] and outputs from local meteorological models constrained by local data collection [*Wadge et al.*, 2002; *Foster et al.*, 2006; *Puysségur et al.*, 2007; *Foster et al.*, 2013]. These methods have had mixed success as they rely on the collection of external data, co-located in space and time, which are not always available for the time of each SAR acquisition. As one needs to consistently correct each interferogram to minimize errors and biases in time series reconstructions or estimates of regional strain rates, the availability of independent meteorological data is a major limitation.

Recently, several studies focused on the use of Global Atmospheric Models (hereafter GAMs) to predict delays at the time of SAR acquisitions and correct for the stratified tropospheric delays [e.g. *Doin et al.*, 2009; *Jolivet et al.*, 2011]. Based on the reanalysis of global meteorological data, these models provide estimates of atmospheric variables, including temperature, water vapor partial pressure and geopotential height of pressure levels, on a regular spatial grid (global or regional) at regular time steps. Following *Doin et al.* [2009], who validated the potential of GAMs by showing quantitative comparisons of empirical corrections and GAMs outputs, *Jolivet et al.* [2011] developed a predictive, systematic, correction tool using GAMs. We build on these later studies to explore in greater detail the prediction of stratified tropospheric delays from GAMs.

In this study, we rely on three GAMs, ERA-Interim [European Center for Medium-Range Weather Forecasts (hereafter ECMWF), *Dee et al.*, 2011], the North American Regional Reanalysis (hereafter NARR) [National Center for Environmental Prediction, *Mesinger et al.*, 2006] and the Modern Era-Retrospective Analysis (hereafter MERRA) [NASA *Rienecker et al.*, 2011], to explore the effects of such corrections in different geographical and tectonic environments.

We begin with a description of our method including modifications to our original implementation and show the importance of estimating the full propagation delay, accounting for the spatio-temporal variations of both water vapor and temperature (i.e. wet delay) and pressure (i.e. hydrostatic or dry delay). We validate this approach with measurements of the integrated precipitable water vapor using the Medium Resolution Imaging Spectrometer (MERIS), a passive spectrometer onboard the ENVISAT satellite. We discuss the effect of turbulence on the quality of the predictions from GAMs. We also present examples highlighting the variable performances of different reanalysis products.

Using 4 different examples, we highlight:

1. The ability to predict lateral variations in delays along a coastal area and across a major mountain range (example from Northern Chile),

2. The potential for prediction of long wavelength phase delays (example from Makran),

3. Improvement in the measurement of earthquake-related ground deformations (example from the 2005 Mw 7.7 Tarapacá earthquake),

4. The importance of tropospheric correction on time series reconstructions and velocity estimates (example from a time series of deformation on the flank of Mt. Etna from 2003 to 2010).

Unless otherwise specified, the interferograms shown in this study have been processed from raw data to an unwrapped geocoded product using the ROI_PAC InSAR processing software suite following the standard 2-pass procedure [*Rosen et al.*, 2004]. We use precise orbits and the Shuttle Radar Topography Mission (SRTM) Digital Elevation Model (DEM) with a 90 m pixel spacing [*Farr and Kobrick*, 2000].

2. Computing an atmospheric phase screen from global atmospheric reanalysis

2.1. Method and implementation

The Line-Of-Sight (LOS) tropospheric delay is the integral of air refractivity between the ground and the satellite. Neglecting the compressibility of air and water vapor, the refractivity of air can be written [e.g. *Smith and Weintraub*, 1953]

$$N = k_1 \frac{P_d}{T} + k_2 \frac{e}{T} + k_3 \frac{e}{T^2}, \quad (1)$$

where P_d is the partial pressure of dry air, T is the temperature, e is the partial pressure of water vapor and $k_1 = 0.776$ K.Pa^{-1}, $k_2 = 0.716$ K.Pa-1 and $k_3 = 3.75e3$ K^2.Pa^{-1} are empirical constants determined by *Smith and Weintraub* [1953]. This formulation does not account for the water content of clouds which we assume to be part of the turbulent delay. We also neglect the impact of spatio-temporal variations in ionospheric electronic content. Most of the examples shown in the present study use C-band sensors (wavelength of 5 cm) that are usually minimally affected by such perturbations [*Hanssen*, 2001]. Regardless, ionospheric perturbations are beyond the scope of the present study [for an example of ionospheric perturbations, see *Raucoules and de Michele*, 2010]. The total LOS single path tropospheric delay, $\delta \mathrm{L}_{LOS}^{total}(z,t)$, is derived by integrating the refractivity N between the ground at elevation z and a reference elevation z_{ref} above which spatio-temporal

variations of N are negligible. $\delta \mathrm{L}_{LOS}^{total}(z,t)$ is the sum of the hydrostatic delay, $\delta \mathrm{L}_{LOS}^{dry}(z)$, and the wet delay, $\delta \mathrm{L}_{LOS}^{wet}(z)$ (i.e. the hydrostatic delay is defined as the theoretical delay in the case where the water vapor partial pressure $e(z,t) = 0\,\mathrm{Pa}$, *Doin et al.* [2009]). At a given time t and for a pixel at elevation z, we write

$$\delta \mathrm{L}_{LOS}^{total}(z,t) = \delta \mathrm{L}_{LOS}^{dry}(z,t) + \delta \mathrm{L}_{LOS}^{wet}(z,t), \text{ where} \quad (2)$$

$$\delta \mathrm{L}_{LOS}^{dry}(z,t) = \frac{10^{-6}}{cos(\theta)} \frac{k_1 R_d}{g_m} [P(z,t) - P(z_0,t)], \text{ and} \quad (3)$$

$$\delta \mathrm{L}_{LOS}^{wet}(z,t) = \frac{10^{-6}}{cos(\theta)} \int_z^{z_{ref}} \Big[\Big(k_2 - \frac{R_d}{R_v} k_1 \Big) \frac{e(z,t)}{T(z,t)} + k_3 \frac{e(z,t)}{T(z,t)^2} \Big] dz, \quad (4)$$

where θ is the LOS incidence angle, $P = P_d + e$ is the total pressure, $R_d = 287.05$ J.Kg^{-1}.K^{-1} and $R_v = 461.495$ J.Kg^{-1}.K^{-1} are the specific gas constants for dry air and water vapor, respectively, and g_m is the local gravity at the center of the atmospheric column between z and z_{ref} (here, we fix $g_m = 9.8$ m.s^{-2}) [*Saastamoinen*, 1972]. Thus, given vertical profiles of temperature, pressure and water vapor partial pressure, eq. 2 allows one to compute an estimate of the absolute phase delay for two acquisitions at time t_1 and t_2 and combine them into the interferometric tropospheric phase delay as,

$$\Delta \mathrm{L}_{LOS}^{t_1,t_2}(z) = \delta \mathrm{L}_{LOS}^{s}(z,t_2) - \delta \mathrm{L}_{LOS}^{s}(z,t_1). \quad (5)$$

Global and regional reanalysis of atmospheric data provide estimates of atmospheric variables several times a day at different pressure levels. Here, we consider three different reanalysis, ERA-Interim, NARR and MERRA. ERA-Interim is the latest atmospheric reanalysis of the ECMWF, following ERA-40. It provides estimates of temperature, water vapor partial pressure and geopotential height along 37 pressure levels, on a global 0.7° grid, at 0:00, 6:00, 12:00 and 18:00 UTC daily, from 1989 to present. NARR is a regional model that provides estimates of the same atmospheric variables along 29 pressure levels,

on a Northern Hemisphere Lambert Conformal Conic grid centered on the United States, at 0:00, 3:00, 6:00, 9:00, 12:00, 15:00, 18:00, 21:00 UTC daily, from 1979 to present. MERRA is a global reanalysis, providing the same variables, along 42 pressure levels, on a global grid (0.5° along longitude and 0.75° along latitude), at 0:00, 6:00, 12:00 and 18:00 UTC daily, from 1979 to present. Details on the atmospheric data used as inputs, the assimilation process and the model performances are described in *Dee et al.* [2011] for ERA-Interim, *Mesinger et al.* [2006] for NARR and *Rienecker et al.* [2011] for MERRA. We briefly compare the performance of these three reanalysis in section 2.5.

Jolivet et al. [2011] describe the derivation of maps of path delay, coincident with SAR acquisitions, from the outputs of atmospheric reanalysis. To model the single path delay at an acquisition time t_i, we extract the vertical profiles of temperature, water vapor partial pressure and geopotential height from the reanalysis output the closest to time t_i, at each grid point in an area that encompass the entire SAR scene. We then convert the geopotential height to a regular vertical metric grid, by dividing by g_m. By integrating eqs. 3 and 4, we compute both hydrostatic and wet delay contributions on each grid point. Finally, we use a spline interpolant in the vertical direction to estimate the delay at the pixel's elevation and a bilinear interpolant in the horizontal direction. We then differentiate delay maps at each different time of acquisition to derive the predicted interferometric stratified tropospheric delay.

The method just described is implemented as an open-source, fully-documented, Python-based package, called PyAPS (Python-based Atmospheric Phase Screen), available at `http://www.earthdef.caltech.edu` [*Agram et al.*, 2013]. Among the main modifications from the previous implementation described in *Jolivet et al.* [2011], this package

now allows one to automatically download atmospheric reanalysis products and to produce maps of stratified tropospheric delays for both geocoded and radar geometries using the Digital Elevation Model used in processing the InSAR data. PyAPS can be used with ECMWF's ERA-Interim, NCEP's NARR and NASA's MERRA outputs. We note that additional routines using any global and regional reanalysis can be easily implemented [*Agram et al.*, 2013].

In the present study, we use the SRTM DEM for all delay predictions [*Farr and Kobrick*, 2000]. The reference elevation is set to 30 km as it is the top of the atmospheric layer modeled in both ERA-Interim and NARR. We assume negligible effects due to spatial and temporal variations in atmospheric stratification above this reference elevation.

2.2. The importance of estimating the hydrostatic delay

At the scale of an interferogram, the spatial variations of pressure are usually small (i.e. typically within an order of magnitude of 1 hPa), while larger variations of water vapor partial pressure are common. As a consequence, the differential wet delay usually overwhelms the differential hydrostatic delay. Therefore, most efforts have focused on predicting the wet delay component [e.g. *Li et al.*, 2006a, 2012], but very few studies also include an accurate hydrostatic delay estimate [e.g. *Foster et al.*, 2006; *Puysségur et al.*, 2007]. The hydrostatic delay can be estimated using continuous GPS stations, local collection of meteorological data with weather balloons or dynamic modeling of the atmosphere, or can be approximated from the ground pressure, following *Saastamoinen* [1972] [*Delacourt et al.*, 1998]. Using GAMs, we provide an efficient and accurate approach to predict hydrostatic delay that can be combined with estimates of wet delay to predict the total tropospheric stratified delay.

Figure 1 shows a 35-day interferogram covering an area in southern California, extending from the Mojave Desert in the north to the Los Angeles Basin area in the south. The average perpendicular component of the interferometric baseline, $B_\perp$, is 136 m. Because of the short temporal baseline, we consider that deformation signals are negligible, although strong, localized, vertical displacements are reported throughout the Los Angeles basin area [southern part of the interferogram; *Bawden et al.*, 2001]. We compare the unwrapped interferogram with both the wet and hydrostatic delay predicted using outputs from ERA-Interim. In Figure 2, we show the interferometric phase as a function of elevation.

The prediction, based on ERA-Interim, reproduces the observed phase in the interferogram reasonably well (Fig. 1 and Fig. 2c.) with a $\sim$70% reduction in variance without orbit re-estimation. Some atmospheric signal remains, especially north of the San Gabriel Mountains (118^o W, 34.6^o N), but the long wavelength signal is well explained by a change in the delay/elevation function from the Sierra Nevada mountains to the north, to the lower elevation Mojave Desert in the center, and the coastal Los Angeles Basin to the south. The variance reduction when only the wet delay is taken into account is approximately 55%. As shown in Fig. 1 and Fig. 2, the hydrostatic delay should not be neglected as it accounts for about 15% of the variance reduction.

2.3. Validation using independent measurements of atmospheric integrated water vapor content from MERIS

Jolivet et al. [2011] did not validate the correction method against independent measurements of any atmospheric variables. Here, we take advantage of the Medium Resolution Imaging Spectrometer instrument (MERIS), a passive multi-spectral imager with 15 bands ranging from 395 nm to 900 nm. This instrument was onboard the European

Space Agency's Envisat satellite and acquired data at the same time as the Advanced Synthetic Aperture Radar (ASAR). *Fischer et al.* [1997] describe how to derive maps of the precipitable water vapor at a 300 m spatial resolution from the ratio of radiances at bands 14 (885 nm) and 15 (900 nm), when no clouds mask the ground. When MERIS data has been acquired simultaneously with a SAR image, the derived precipitable water vapor maps can be used to produce maps of the wet delay with unprecedented resolution [e.g. *Li et al.*, 2006b; *Puysségur et al.*, 2007; *Li et al.*, 2012].

We follow the methodology proposed by *Li et al.* [2012] to derive maps of the tropospheric wet delay from the MERIS precipitable water vapor. We use the MERIS cloud mask product to discard areas covered by clouds. Such areas will not be included in further analysis. We write $\delta \mathrm{L}_{LOS}^{wet}$ as,

$$\delta \mathrm{L}_{LOS}^{wet} = \frac{\Pi}{\cos\theta} W_{prec}, \tag{6}$$

where W_{prec} is the MERIS derived precipitable water vapor, θ is the Line-Of-Sight incidence angle and Π is a non-dimensional mapping factor given by *Bevis et al.* [1994] as,

$$\Pi = 10^{-6} \rho R_v \big[\frac{k_3}{T_m} + k_2 - w k_1 \big], \tag{7}$$

where ρ is the density of liquid water, w is the ratio of molecular masses of water vapor and dry air ($\sim$0.668) and $T_m(z)$ is a weighted average of the temperature between the ground and a reference altitude, given by, for a pixel at an altitude z,

$$T_m(z) = \frac{\int_z^{z_{ref}} e/T dz}{\int_z^{z_{ref}} e/T^2 dz}. \tag{8}$$

We evaluate the weighted average temperature at each pixel of the radar scene using the outputs from ERA-Interim to produce a map of Π. We then produce maps of the MERIS

derived wet delay by multiplying the MERIS precipitable water vapor by Π. Values of Π typically range from 5 to 7 [*Li et al.*, 2012].

We compare the performance of the MERIS derived and ERA-Interim derived predictions of the wet delay on an interferogram computed using two SAR acquisitions on 08/27/2004 and 05/03/2004 by the Envisat satellite over the eastern Makran region in Pakistan (Fig. 3). The average $B_\perp$ is 235 m. The pixel size is $\sim$ 600 m (i.e. 32 and 160 looks applied along azimuth and range, respectively). The covered area extends from the coast of the Indian ocean to the Baluchistan desert. The expected deformation rates due to nearby subduction are poorly constrained but are not likely to be higher than a few mm/yr [*Byrnes et al.*, 1992]. We therefore consider the 4 months interferogram shown here to be free of any significant tectonic deformation signal and to reflect the spatial and temporal variations of tropospheric stratification.

The prediction of wet delay from ERA-Interim and MERIS show a good agreement, with a difference of standard deviation of 1.3 cm along the LOS. Topographic related patterns visible in the south are well predicted using both techniques. We derive the total LOS delay from MERIS and ERA-Interim by adding the LOS hydrostatic delay derived from ERA-Interim in order to validate our approach with the data. The standard deviation of the residuals after correcting with MERIS is about 4.4 cm and 5.4 cm after correcting with ERA-Interim. These values drop to 0.6 cm and 1.0 cm, respectively, when removing a 2-D best-fitting linear ramp to account for orbital uncertainties (Fig. 3). Additional examples of successful and less successful corrections are shown in Supplementary Materials.

We repeat this evaluation of the reduction of standard deviation, including the orbital estimation, on 31 interferograms with a temporal baseline of less than 1 year computed

on orbital track 449 covering the Pakistani Makran area. Our analysis is restricted to cases where the cloud coverage is of less than 30% of the scene. We compare the standard deviation of the original interferogram to that of the interferogram corrected for total tropospheric delays derived from MERIS and ERA-Interim, both with and without a 2-D best-fit linear function removed to account for potential orbital inaccuracies (Fig. 4). Corrections based on MERIS delay maps lead to a reduction of standard deviation in 30 cases out of 31. MERIS does not lead to a reduction of standard deviation in all cases because of variable cloud coverage. ERA-Interim delay maps lead to a variance reduction in 28 cases out of 31. Including the estimation and removal of a 2-D best-fit linear function leads to a reduction of standard deviation in all cases with MERIS and ERA-Interim. Similarly to what has been observed over Tibet by *Jolivet et al.* [2011], delay corrections derived from ERA-Interim never produce any significant increase of the phase standard deviation and the standard deviation of the corrected product is, in the end, relatively stable for all interferograms ($\sim 1-2$ cm, Fig. 4).

Our analysis confirms that MERIS is more accurate than reanalysis predictions and should be used whenever daytime cloud-free data are available, as shown by recent studies [*Walters et al.*, 2013; *Lin*, 2013]. The temperature and pressure vertical profiles provided by GAMs should be used in addition to the water vapor measurement to estimate the mapping factor Π and to derive the hydrostatic component of the delay. Still, the total delay predicted from ERA-Interim shows performances similar to that predicted using MERIS and should be used when no other independent data are available.

2.4. Troposphere stratification and turbulences

Jolivet et al. [2011] describe an 73% average reduction in APS using the ERA-Interim correction over all the short temporal baseline interferograms covering the Kunlun Fault area. Such a performance is quite acceptable, but understanding the reasons leading to poor predictions of the tropospheric delay is key. To what extent global or regional atmospheric models accurately predict tropospheric delay is primarily controlled by the level of turbulence in the lower troposphere at the time of the SAR acquisitions.

As a proxy for the ratio between turbulent and stratified delays, we estimate the coefficient of correlation between interferometric phase and elevation. When this coefficient of correlation differs significantly from zero, topography correlates with the interferometric phase, suggesting significant stratification of the troposphere, hence a relatively low level of turbulence. In Fig. 5, we represent the coefficient of correlation between phase and topography as a function of the standard deviation of the residuals after correcting the interferogram from the delay predicted with ERA-Interim. These examples are from Envisat acquisitions over two tracks covering the Pakistani Makran. As suggested by the two ellipses that enclose 90% of the data, when the applied correction decreases the interferogram variance (i.e. the synthetic delay reproduces the interferometric phase), it is statistically associated with a correlation between phase and topography (i.e. low turbulence).

An example of turbulence overprinting of the tropospheric stratification signal is shown by the ERS-1 interferogram covering the region around Parkfield, California, USA (Fig. 6). The temporal baseline is 35 days and the average $B_{\perp}$ is 125 m. The area extends from the Pacific coast in the south-west, to the Great Valley of California in the north-east.

We compare this interferogram with the stratified tropospheric delay predicted from the outputs of NARR (Fig. 6). Some patterns that match with the topography are correctly predicted using NARR (black arrows on Fig. 6). However, some of the predicted patterns are not visible in the interferogram. The dashed line roughly represents the limit between two domains. To the southwest, phase and topography correlate, while to the northeast, no clear correlation is visible. The region closer to the ocean also does not show a clear correlation. When no clear correlation is visible, the phase patterns look turbulent (i.e. following a spatially random distribution). In these cases, our method fails to improve the observations. By definition, we cannot predict perturbations with a wavelength smaller than the spacing between atmospheric model grid points (Fig. 6).

2.5. Comparing different reanalysis

We briefly compare the predictions from three GAMs: NARR, ERA-I and MERRA. Figure 7 shows a 46 days ALOS interferogram covering the Kilauea volcano, Hawaii. The average perpendicular baseline is $\sim$190 m. All three reanalysis reproduce the gross features of the spatial variations in phase over the volcano, with a reduction of standard deviation of 83%, 27% and 27% for NARR, ERA-Interim and MERRA, respectively. In this particular case, NARR performs significantly better as it predicts the phase/elevation relationship on low elevation terrains, where ERA-Interim and MERRA fail.

Extending this comparison to all the interferograms used in this study and a few additional interferograms (see table in Supplementary Materials), we compare the standard deviation after correcting for the total delay predicted from ERA-Interim and MERRA, including the effect of an additional 2-D best-fit linear function to account for potential long-wavelength artifacts induced by imprecise orbit knowledge (Fig 8). While the num-

ber of interferograms used here are probably not a statistically representative sample, the trend suggests that one cannot chose systematically between ERA-Interim or MERRA, as their performances are relatively similar. As NARR only covers the North American continent, we did not include it in this comparison. From our experience, performance of each GAM has to be examined on a case-by-case basis on short temporal baseline interferograms.

3. Application to case studies

We present 4 cases where the use of GAMs to predict the interferometric delay related to tropospheric stratification is essential to accurately measure ground deformation.

3.1. From a coastline to high mountains, the example of Northern Chile

Lateral variations in the tropospheric stratification leading to lateral changes in the phase/elevation relationship are not usually captured by empirical methods, whereas they can be reproduced using GAMs [*Jolivet et al.*, 2011]. Furthermore, most empirical methods cannot track such variability over a relatively flat terrain such as along a coastline. Predicting the spatial variability of atmospheric phase delay is key, for instance when tracking the lateral variations of coupling along a subduction zone [e.g. *Béjar-Pizarro et al.*, 2013].

To illustrate this problem, we use a ∼7 month interferogram covering about 400 km along the northern Chile coastline and extending further north in the Andes over the Atacama Plateau (Fig. 9). The average $B_\perp$ is ∼100 m. The phase versus elevation relationship can be approximated by a simple quadratic form over 1500 m of elevation

(bottom of Fig. 9). However, this relationship breaks down below 1000 m where a strong N-S variations in phase appears relatively uncorrelated with topography.

The predicted delay computed using ERA-Interim gives a reasonable estimate of delay across the entire scene with a variance reduction of ∼86%. The trend for elevations higher than 1500 m is reproduced together with the broad distribution of values at low elevation. This variability is due to a long wavelength atmospheric change along the Pacific Coast, from north to south, that is well described in ERA-Interim. This example shows the potential for estimating and correcting long wavelength atmospheric fluctuations using GAMs even on relatively flat terrains.

3.2. Estimating long wavelength deformations

Observing long wavelength deformation signals is a quite challenging task using InSAR because of the multiplicity of long wavelength noise sources in the interferometric phase. Long wavelength deformation signals, such as those expected along a subduction zone for instance [e.g. *Béjar-Pizarro et al.*, 2013], can trade off with inaccurate satellite orbits, oceanic tidal load signals [*DiCaprio and Simons*, 2008], hydrological load signals [*Fu et al.*, 2012] and long wavelength variations in atmospheric stratification. Therefore, orbital parameters, which mimic long wavelength phase variations, are often estimated during the inversion for tectonic parameters (i.e. slip rate, slip distributions...), introducing more variability in the inversion process.

We illustrate this case with a 70-day interferogram covering eastern Makran, in Pakistan. The average $B_\perp$ is 235 m. We have applied two corrections to this interferogram. We predict the stratified tropospheric delay using the ERA-Interim reanalysis and correct the interferogram for this delay (Fig. 10, Top). Independently, we fit a linear plane on the

original interferogram as an approximation of a residual orbital signal (Fig. 10, bottom). The two sets of corrections perform similarly. The variance reduction by correcting for the stratified delay is ∼48% while it is ∼54% including the correction for an orbital plane.

As shown by *DiCaprio and Simons* [2008], oceanic tidal load signals can be modeled and removed, while models are currently being developed to predict the influence of seasonal hydrological load on continents [e.g. *Fu et al.*, 2012]. As a consequence, by using external data, such as GPS [e.g. *Tong et al.*, 2013; *Béjar-Pizarro et al.*, 2013], to constrain the residual orbital errors, or as the quality of estimated orbits should drastically increase with the future SAR missions, our method will allow one to decipher between long wavelength atmospheric signals and long wavelength deformation signals.

3.3. The case of an earthquake

Often, in the case of an earthquake, ground deformation is so large that it overprints the atmospheric signal [e.g. *Massonnet et al.*, 1992; *Jònsson et al.*, 2002; *Simons et al.*, 2002]. However, atmospheric perturbations affect the measurements, as shown for ionospheric disturbance in L-band coseismic interferograms [*Shen et al.*, 2009; *Raucoules and de Michele*, 2010]. Here, we evaluate the case of a coseismic interferogram in which the deformation signal is greatly perturbed by tropospheric stratification.

The June 13th, 2005, Mw 7.7 Tarapacá earthquake was an intra-slab normal event with a hypocenter located at about 98 km depth in the Pacific subducting plate in northern Chile [*Peyrat et al.*, 2006]. We compute two interferograms using Envisat ASAR acquisitions on the adjacent orbital tracks 96 and 368 covering similar time spans (Fig. 11). Both interferograms are quite different. Especially, the phase gradient on the western side on the bull's eye-shape deformation pattern differs between the two images. Such differences

can yield ambiguities in modeling the size and depth of such an earthquake. However, this phase gradient is coincident with a step in elevation along the cordillera and is well predicted using the ERA-Interim reanalysis (center panels on Fig. 11). The atmospheric prediction on track 368 shows no delay due to stratification of the troposphere, while a strong signal is visible on the track 96 interferogram. When corrected for the predicted stratified tropospheric delay and after adjusting for a constant offset, both interferograms match in the overlapping area (note that the LOS angle is not exactly the same in the area of overlap).

In their study, *Peyrat et al.* [2006] estimate empirically a linear phase/elevation relationship, removing 2-5 cm of delay. Our approach reproduces their relationship. After correction, the total range change between the center of the bull's eye shaped deformation field and the coastline reaches 18-20 cm. In this case, as the phase/elevation relationship is simple (i.e. linear), the empirical approach has proven successful. Using GAMs and a direct forward modeling of the tropospheric delay, we avoid the possible trade-offs between deformation and topography-correlated atmospheric delays.

3.4. Removing periodic oscillations in phase measurement for time series reconstruction

We can use GAMs to correct single interferograms if one intends to observe and model rapid, large-amplitude, deformation signals. However, the detection of low amplitude deformation signals, such as interseismic deformation [e.g. *Elliott et al.*, 2008; *Cavalié et al.*, 2008; *Jolivet et al.*, 2012; *Béjar-Pizarro et al.*, 2013] or long lasting subsidence [e.g. *Cavalié et al.*, 2007], requires interferogram stacking or time series analysis. Time series analysis methods have proven successful in mitigating turbulent atmospheric signals [e.g *Ferretti*

et al., 2001; *Berardino et al.*, 2002; *Cavalié et al.*, 2007; *Hooper et al.*, 2007; *Hetland et al.*, 2012]. Such methods assume the atmospheric phase screen is random in time and use spatial [e.g. *Ferretti et al.*, 2001; *Berardino et al.*, 2002] and/or temporal filters [e.g. *Schmidt et al.*, 2005; *Cavalié et al.*, 2007; *Agram et al.*, 2013] to reduce biases in strain rate estimates and time series reconstruction. However, as the stratified tropospheric delay is not randomly distributed in space, it cannot be filtered out by spatial averaging. Additionally, as shown by *Doin et al.* [2009], seasonal oscillations of the stratified tropospheric delay might be aliased in estimates of strain rates because of uneven temporal sampling of SAR acquisitions. We illustrate the effect of correcting for the stratified tropospheric delay on the Envisat time series of SAR data covering Mt. Etna, from 2003 to 2010.

We use the dataset processed and described in *Doin et al.* [2009]. 222 interferograms have been generated using the NSBAS processing chain, together with ROI_PAC [*Rosen et al.*, 2004], combining 63 SAR ascending acquisitions covering Mt. Etna between January 2003 and June 2010. Using the Generic Interferometric Analysis Toolbox (GIAnT), we derive a time series of displacement and a displacement rate map [*Agram et al.*, 2013]. Stratified tropospheric delay predictions are derived from the ERA-Interim reanalysis. We flatten all interferograms by removing a best-fitting orbital function linear in range and azimuth. The orbital parameters are consistently re-estimated in a least-square sense within the interferometric network. We use the NSBAS inversion method to derive each pixel's LOS deformation evolution between 2003 and 2010 and a map of the average range change. Details about the time series inversion method can be found in *Lopez-Quiroz et al.* [2009] and *Jolivet et al.* [2012].

In the following, we compare the reconstructed time series and the velocity maps obtained with and without using tropospheric corrections. We first focus on the comparison between the average velocity field over the 2003-2010 period, obtained with and without correcting for the stratified tropospheric delay on each interferogram. The difference between both velocity fields (hereafter called a velocity bias) is shown on Fig. 12a. and its relationship with topography is shown on Fig. 12b.

The velocity bias is $\sim$4 mm/yr between the bottom and the top of the volcanic cone. As the deformation rates are on the order of the centimeter per year, such variation can affect our interpretation of subsurface processes. Furthermore, the bias shows a correlation with the topography (Fig. 12). As the expected deformation field due to magma storage at depth is radial spreading centered on the volcanic edifice [e.g. *Lundgren et al.*, 2004], one should account for the stratified tropospheric delays over Mt. Etna (as originally suggested by *Delacourt et al.* [1998]). The use of GAMs makes this correction relatively straight forward.

The difference in velocity fields with and without atmospheric correction is due to the aliasing of seasonal oscillations in the phase change rate associated with the uneven temporal sampling of SAR acquisitions. In figure 12c., we show the temporal evolution of a group of pixels located next to the top of Mt. Etna (Fig. 12d.), comparing the displacements with and without applying a stratified tropospheric correction derived from ERA-Interim. Together with the phase values we plot a filtered time series for both cases, using a 75 days, low pass, Gaussian filter. We clearly see the effects of the tropospheric corrections on the temporally smoothed time series. The seasonal signal, visible in the uncorrected time series (in black), is partially removed with the correction (in blue).

By fitting the sum of a sine and cosine function, with an annual periodicity, to the raw, unfiltered pixel's time series with and without atmospheric corrections, we can examine the spatial distribution of the seasonal oscillations reduction (Fig. 12d.). For each independent pixel, we use a least square approach to estimate the amplitudes of the seasonal oscillations a and b, related to $\varphi(t)$, the phase evolution at time t, by,

$$\varphi(t) = a\sin(t) + b\cos(t), \tag{9}$$

with the amplitude of the annual oscillation given as $\sqrt{a^2 + b^2}$. We estimate this amplitude on the time series reconstructed with and without atmospheric corrections. The amplitude difference in the seasonal oscillation is correlated with the topography, as is the velocity bias (Fig. 12d.). We conclude that the velocity difference observed in Fig. 12a. is indeed due to seasonal oscillations of the stratified tropospheric delay that were aliased into the rate of range change.

4. Conclusion

We present here further validation of the use of GAMs to correct interferograms for stratified tropospheric delays. The presented examples emphasize the potential of this approach for an automatic, systematic, prediction of the stratified delay in InSAR. This method is not suited for estimating turbulent patterns on single interferograms. More direct approaches can and should be used when available, such as GPS derived zenith delays or using the collection of atmospheric data. Still, GAMs can be used for any SAR acquisition, especially when no external datasets are available. Furthermore, from our validation and those provided by *Jolivet et al.* [2011], it seems that this correction never significantly increases the noise level in interferograms. Yet, in order to assess to

what extent this correction method can be applied systematically, a study of the global variability of the performances of the method is still needed (i.e. is there geographical region where this method succeeds/fails systematically?).

By removing the stratified tropospheric delay, improvements are multiple. Unwrapping is greatly improved over rough terrains where the interferometric phase may be aliased [*Grandin et al.*, 2012]. Lateral variations in stratification can be resolved, allowing in certain cases a decrease in existing trade-offs between the long wavelength deformation signals and the different sources of noise. The accuracy of our measurements in the case of an earthquake is improved. Finally, it allows one to mitigate bias in velocity field estimates by decreasing the amplitude of seasonal oscillations in the reconstructed phase while using time series analysis. These corrections should become standard in processing of InSAR data, especially since it is free, automatic and always available.

Acknowledgments. We would like to thank two anonymous reviewers for their fruitful comments and suggestions and the associate editor for his help in evaluating this paper. We also would like to thanks Simona Bordoni (Caltech) for all the discussions about the Global Atmospheric Models used in this study. Part of G. Peltzer's contribution was done at the Jet Propulsion Laboratory, California Institute of Technology under contract with NASA. Figures and maps were prepared using Generic Mapping Tools software [*Wessel and Smith*, 1995]. This study has been funded by NSF grant EAR-1118239. This is Caltech Seismo lab contribution N°10096. This is TO contribution N°252.

References

Agram, P. S., R. Jolivet, B. Riel, Y. N. Lin, M. Simons, E. Hetland, M. P. Doin, and C. Lasserre (2013), New Radar Interferometric Time Series Analysis Toolbox Released, *Eos*, *94*(7), 69–76, doi:10.1029/2011JB008731.

Bawden, G. W., W. Thatcher, R. S. Stein, K. Hudnut, and G. Peltzer (2001), Tectonic contraction across los angeles after removal of groundwater pumping effects, *Nature*, *412*, 812–815, doi:10.1038/35090558.

Beauducel, F., P. Briole, and J. Froger (2000), Volcano-wide fringes in ERS synthetic aperture radar interferograms of Etna (1992-1998): Deformation or tropospheric effect?, *J. Geophys. Res.*, *105*(B7), 16,391–16,402.

Béjar-Pizarro, M., A. Socquet, R. Armijo, D. Carrizo, J. Genrich, and M. Simons (2013), Interseismic coupling and andean structure in the north chile subduction zone, *Nat. Geosci.*, *6*(1), doi:10.1038/ngeo1802.

Berardino, P., G. Fornaro, R. Lanari, and E. Santosti (2002), A new algorithm for surface deformation monitoring based on small baseline differential sar interferograms, *IEEE Trans. Geosc. Rem. Sens.*, *40*(11), doi:10.1109/TGRS.2002.803792.

Bevis, M., S. Businger, S. Chiswell, T. Herring, R. A. Anthes, C. Rocken, and W. R (1994), GPS meteorology: Mapping zenith wet delays onto precipitable water, *J. App. Meteorol.*, *33*, 379–386.

Byrnes, D. E., L. R. Sykes, and D. M. Davis (1992), Great thrust earthquakes and aseismic slip along the plate boundary of the Makran subduction zone, *J. Geophys. Res.*, *97*(B1), 449–478, doi:10.1029/91JB02165.

513 Cavalié, O., M. P. Doin, C. Lasserre, and P. Briole (2007), Ground motion measurement
514 in the Lake Mead area, Nevada, by differential synthetic aperture radar interferometry
515 time series analysis: Probing the lithosphere rheological structure, *J. Geophys. Res.*,
516 *112*(B3), doi:10.1029/2006JB004344.

517 Cavalié, O., C. Lasserre, M. P. Doin, G. Peltzer, J. Sun, X. Xu, and Z. K. Shen (2008),
518 Measurement of interseismic strain across the Haiyuan fault (Gansu, China), by InSAR,
519 *Earth Planet. Sci. Lett.*, *275*(3-4), 246–257, doi:10.1016/j.epsl.2008.07.057.

520 Dee, D. P., S. M. Uppala, A. J. Simmons, P. Berrisford, P. Poli, S. Kobayashi, U. Andrae,
521 M. A. Balmaseda, G. Balsamo, P. Bauer, P. Bechtold, A. C. M. Beljaars, L. van de Berg,
522 J. Bidlot, N. Bormann, C. Delsol, R. Dragani, M. Fuentes, A. J. Geer, L. Haimberger,
523 S. B. Healy, H. Hersbach, E. V. Hólm, L. Isaksen, P. Kållberg, M. Köhler, M. Ma-
524 tricardi, A. P. McNally, B. M. Monge-Sanz, J. J. Morcrette, B. K. Park, C. Peubey,
525 P. de Rosnay, C. Tavolato, J. N. Thépaut, and F. Vitart (2011), The ERA-Interim
526 reanalysis: configuration and performance of the data assimilation system, *Q. J. R.*
527 *Meteorol. Soc.*, *137*(656), 553–597, doi:10.1002/qj.828.

528 Delacourt, C., P. Briole, and J. Achache (1998), Tropospheric corrections of SAR inter-
529 ferograms with strong topography. Application to Etna, *Geophys. Res. Lett.*, *25*(15),
530 2849–2852, doi:10.1029/98GL02112.

531 DiCaprio, C. J., and M. Simons (2008), Importance of ocean tidal load corrections for
532 differential InSAR, *Geophys. Res. Lett.*, *35*(22), L22,309, doi:10.1029/2008GL035806.

533 Doin, M. P., C. Lasserre, G. Peltzer, O. Cavalie, and C. Doubre (2009), Cor-
534 rections of stratified tropospheric delays in SAR interferometry: Validation with
535 global atmospheric models, *J. App. Geophys.*, *69*(1, Sp. Iss. SI), 35–50, doi:

10.1016/j.jappgeo.2009.03.010.

Doubre, C., and G. Peltzer (2007), Fluid-controlled faulting process in the Asal Rift, Djibouti, from 8 yr of radar interferometry observations, *Geology*, *35*(1), 69–72, doi: 10.1130/G23022A.1.

Elliott, J. R., J. Biggs, B. Parsons, and T. J. Wright (2008), Insar slip rate determination on the altyn tagh fault, northern tibet, in the presence of topographically correlated atmospheric delays, *Geophys. Res. Lett.*, *35*(12), doi:10.1029/2008GL033659.

Emardson, T. R., M. Simons, and F. H. Webb (2003), Neutral atmospheric delay in interferometric synthetic aperture radar applications: Statistical description and mitigation, *J. Geophys. Res.*, *108*(B5), doi:10.1029/2002JB001781.

Farr, G., T., and M. Kobrick (2000), Shuttle radar topography mission produces a wealth of data, *Eos Trans. AGU*, *81*(48), 583–585.

Ferretti, A., C. Prati, and F. Rocca (2001), Permanent Scatterers in SAR Interferometry, *Geosci. Rem. Sens.*, *39*(1), 8–20.

Fischer, J., R. Leinweber, and R. Preusker (1997), Retrieval of Total Water Vapour Content from MERIS Measurements Algorithm Theoretical Basis Document, *ATBD 2.4, European Space Agency*, *4.2*.

Foster, J., B. Brooks, T. Cherubini, C. Shacat, S. Businger, and C. L. Werner (2006), Mitigating atmospheric noise for InSAR using a high resolution weather model, *Geophys. Res. Lett.*, *33*(16), L16,304, doi:10.1029/2006GL026781.

Foster, J., J. Kealy, T. Cherubini, S. Businger, Z. Lu, and M. Murphy (2013), The utility of atmospheric analyses for the mitigation of artifacts in InSAR, *J. Geophys. Res.*, *118*(2), 748–758, doi:10.1002/jgrb.50093.

559 Fu, Y., J. T. Freymueller, and T. Jensen (2012), Seasonal hydrological loading in south-
560 ern Alaska observed by GPS and GRACE, *Geophys. Res. Lett.*, *39*(15), L15,310, doi:
561 10.1029/2012GL052453.

562 Grandin, R., A. Socquet, M.-P. Doin, E. Jacques, B. de Chabalier, and G. C. P.
563 King (2010), Transient rift opening in response to multiple dike injections in the
564 Manda Hararo rift (Afar, Ethiopia) imaged by time-dependent elastic inversion of
565 interferometric synthetic aperture radar data, *J. Geophys. Res.*, *115*(B09403), doi:
566 10.1029/2009JB006883.

567 Grandin, R., M.-P. Doin, L. Bollinger, B. Pinel-Puysségur, G. Ducret, R. Jolivet, and
568 S. Sapkota (2012), Long-term growth of the Himalay inferred from interseismic InSAR
569 measurement, *Geology*, *40*(12), 1059–1062, doi:10.1130/G33154.1.

570 Hanssen, R. F. (2001), *Radar Interferometry, Data Interpretation and Error Analysis*,
571 Remote Sensing and Digital Image Processing, Kulwer Academic Publishers.

572 Hetland, E. A., P. Musé, M. Simons, Lin, P. S. Agram, and C. J. DiCaprio (2012),
573 Multiscale InSAR Time Series (MInTS) analysis of surface deformation, *J. Geophys.*
574 *Res.*, *117*(B2), doi:10.1029/2011JB008731.

575 Hooper, A., P. Segall, and H. Zebker (2007), Persistent scatterer interferometric synthetic
576 aperture radar for crustal deformation analysis, with application to Volcan Alcedo,
577 Galapagos, *J. Geophys. Res.*, *112*(B7), doi:10.1029/2006JB004763.

578 Jolivet, R., R. Grandin, C. Lasserre, M.-P. Doin, and G. Peltzer (2011), Systematic
579 InSAR tropospheric phase delay corrections from global meteorological reanalysis data,
580 *Geophys. Res. Lett.*, *38*(17), doi:10.1029/2011GL048757.

Jolivet, R., C. Lasserre, M.-P. Doin, S. Guillaso, G. Peltzer, R. Dailu, and J. Sun (2012), Shallow creep on the haiyuan fault revealed by insar, *J. Geophys. Res.*, *117*(B6), doi: 10.1029/2011JB008732.

Jònsson, S., H. A. Zebker, P. Segall, and F. Amelung (2002), Fault slip distribution of the 1999 Mw7.1 Hector Mine, California, earthquake, estimated from satellite radar and GPS measurements, *Bull. Seismol. Soc. Am.*, *92*(4), 1377–1389, doi: 10.1785/0120000922.

Lasserre, C., G. Peltzer, F. Crampe, Y. Klinger, J. Van der Woerd, and P. Tapponnier (2005), Coseismic deformation of the 2001 Mw=7.8 Kokoxili earthquake in Tibet, measured by synthetic aperture radar interferometry, *J. Geophys. Res.*, *110*(B12), doi: 10.1029/2004JB003500.

Li, Z., E. J. Fielding, P. Cross, and J.-P. Muller (2006a), Interferometric synthetic aperture radar atmospheric correction: GPS topography-dependent turbulence model, *J. Geophys. Res.*, *111*(B02404), doi:10.1029/2005JB003711.

Li, Z., E. J. Fielding, P. Cross, and J.-P. Muller (2006b), Interferometric synthetic aperture radar atmospheric correction: Medium Resolution Imaging Spectrometer and Advanced Synthetic Aperture Radar integration, *Geophys. Res. Lett.*, *33*(6), doi: 10.1029/2005GL025299.

Li, Z., E. J. Fielding, P. Cross, and R. Preusker (2009), Advanced InSAR atmospheric correction: MERIS/MODIS combination and stacked water vapour models, *Int. J. Remote Sens.*, *30*(13), 3343–3363, doi:10.1080/01431160802562172.

Li, Z. W., W. B. Xu, G. C. Feng, J. Hu, C. C. Wang, X. L. Ding, and J. J. Zhu (2012), Correcting atmospheric effects on InSAR with MERIS water vapour data and elevation-

dependent interpolation model, *Geophys. J. Int.*, *189*(2), 898–910, doi:10.1111/j.1365-246X.2012.05432.x.

Lin, Y. N. (2013), Using space geodesy to constrain variations in seismogenic behavior on subduction megathrusts, Ph.D. thesis, California Institute of Technology.

Lin, Y. N., M. Simons, E. A. Hetland, P. Muse, and C. DiCaprio (2010), A multi-scale approach to estimating topographically-correlated propagation delays in radar interferograms, *Geochem. Geophys. Geosys.*, *11*(Q09002), doi:10.1029/2010GC003228.

Lopez-Quiroz, P., M.-P. Doin, F. Tupin, P. Briole, and J.-M. Nicolas (2009), Time series analysis of Mexico City subsidence constrained by radar interferometry, *J. App. Geophys.*, *69*(1, Sp. Iss. SI), 1–15, doi:10.1016/j.jappgeo.2009.02.006.

Lundgren, P., F. Casu, M. Manzo, A. Pepe, P. Berardino, E. Sansosti, and R. Lanari (2004), Gravity and magma induced spreading of Mount Etna volcano revealed by satellite radar interferometry, *Geophys. Res. Lett.*, *31*(4), L04,602, doi:10.1029/2003GL018736.

Massonnet, D., M. Rossi, C. Carmona, F. Adragna, G. Peltzer, K. Feigl, and T. Rabaute (1992), The displacement field of the landers earthquake mapped by radar interferometry, *Nature*, *364*, 138–142.

Mesinger, F., G. DiMego, E. Kalnay, K. Mitchell, P. C. Shafran, W. Ebisuzaki, D. Jović, J. Woollen, E. Rogers, E. H. Berbery, M. B. Ek, Y. Fan, R. Grumbine, W. Higgins, H. Li, Y. Lin, G. Manikin, D. Parrish, and W. Shi (2006), North American Regional Reanalysis, *Bull. Am. Meteorol. Soc.*, *87*(3), 343–360, doi:10.1175/BAMS-87-3-343.

Onn, F., and H. A. Zebker (2006), Correction for interferometric synthetic aperture radar atmospheric phase artifacts using time series of zenith wet delay observations from a

GPS network, *J. Geophys. Res.*, *111*(B9), doi:10.1029/2005JB004012.

Peltzer, G., F. Crampe, S. Hensley, and P. Rosen (2001), Transient strain accumulation and fault interaction in the Eastern California shear zone, *Geology*, *29*(11), 975–978, doi:10.1130/0091-7613(2001)029.

Peyrat, S., J. Campos, J. B. de Chabalier, A. Perez, S. Bonvalot, M. P. Bouin, D. Legrand, A. Nercessian, O. Charade, G. Patau, E. Clévédé, E. Kausel, P. Bernard, and J. P. Vilotte (2006), Tarapacá intermediate-depth earthquake (Mw 7.7, 2005, northern Chile): A slab-pull event with horizontal fault plane constrained from seismologic and geodetic observations, *Geophys. Res. Lett.*, *33*(22), doi:10.1029/2006GL027710.

Pritchard, M. E., and M. Simons (2002), A satellite geodetic survey of large- scale deformation of volcanic centres in the central Andes, *Nature*, *418*, 167–171, doi: 10.1038/nature00872.

Puysségur, B., R. Michel, and J.-P. Avouac (2007), Tropospheric phase delay in interferometric synthetic aperture radar estimated from meteorological model and multispectral imagery, *J. Geophys. Res.*, *112*, doi:10.1029/2006JB004352.

Raucoules, D., and M. de Michele (2010), Assessing ionospheric influence on L-band SAR data: implications on coseismic measurements of the 2008 Sichuan earthquake, *IEEE Geosci. Rem. Sens. Lett.*, *7*(2), 286–290, doi:10.1109/LGRS.2009.2033317.

Rienecker, M. M., M. J. Suarez, R. Gelaro, R. Todling, J. Bacmeister, E. Liu, M. G. Bosilovich, S. D. Schubert, L. Takacs, G.-K. Kim, S. Bloom, J. Chen, D. Collins, A. Conaty, A. da Silva, W. Gu, J. Joiner, R. D. Koster, R. Lucchesi, A. Molod, T. Owens, S. Pawson, P. Pegion, C. R. Redder, R. Reichle, F. R. Robertson, A. G. Ruddick, M. Sienkiewicz, and J. Woollen (2011), MERRA: NASA's Modern-Era Ret-

650 rospective Analysis for Research and Applications, *J. Clim.*, *24*(14), 3624–3648, doi:
651 10.1175/JCLI-D-11-00015.1.

652 Rosen, P., S. Hensley, G. Peltzer, and M. Simons (2004), Updated repeat orbit interfer-
653 ometry package released, *Eos Trans. AGU*, *85*((5)), 47.

654 Ryder, I., B. Parsons, T. J. Wright, and G. J. Funning (2007), Post-seismic motion fol-
655 lowing the 1997 manyi (tibet) earthquake: Insar observations and modeling, *Geophys.*
656 *J. Int.*, *169*, 1009–1027.

657 Saastamoinen, J. (1972), Atmospheric correction for the troposphere and stratosphere in
658 radio ranging of satellites, *AGU Geophysics Monograph Series*, *15*, 247–251.

659 Schmidt, A., D., R. Burgmann, M. Nadeau, R., and M. d'Alessio (2005), Distribution
660 of aseismic slip rate on the Hayward fault inferred from seismic and geodetic data, *J.*
661 *Geophys. Res.*, *110*(B8), doi:10.1029/2004JB003397.

662 Shen, Z.-K., J. Sun, P. Zhang, Y. Wan, M. Wang, R. Bürgmann, Y. Zeng, W. Gan, H. Liao,
663 and Q. Wang (2009), Slip maxima at fault junctions and rupturing of barriers during
664 the 2008 Wenchuan earthquake, *Nat. Geosci.*, *2*(10), 718–724, doi:10.1038/ngeo636.

665 Shirzaei, M., and R. Bürgmann (2012), Topography correlated atmospheric delay correc-
666 tion on radar interferometry using wavelet transforms, *Geophys. Res. Lett.*, *39*(L01305),
667 doi:10.1029/2011GL049971.

668 Simons, M., Y. Fialko, and L. Rivera (2002), Coseismic deformation from the 1999 mw 7.1
669 hector mine, california, earthquake as inferred from insar and gps observations, *Bull.*
670 *Seismol. Soc. Am.*, *92*(4), 1390–1402.

671 Smith, E. K., and S. Weintraub (1953), The constants in the equation for atmospheric
672 refractive index at radio frequencies, in *Proc. I.R.E*, vol. 43, pp. 1035–1037.

673 Tong, X., D. T. Sandwell, and B. R. Smith-Konter (2013), High-resolution Interseismic
674 Velocity Data Along the San Andreas Fault From GPS and InSAR, *J. Geophys. Res.*,
675 *118*, 1–21, doi:10.1029/2012JB009442.

676 Wadge, G., P. Webley, I. James, R. Bingley, A. Dodson, S. Waugh, T. Veneboer,
677 G. Puglisi, M. Mattia, D. Baker, S. Edwards, S. Edwards, and P. Clarke (2002), Atmo-
678 spheric models, GPS and InSAR measurements of the tropospheric water vapour field
679 over Mount Etna, *Geophys. Res. Lett.*, *29*(19), doi:10.1029/2002GL015159.

680 Walters, R. J., J. R. Elliott, B. Parsons, and Z. Li (2013), Rapid strain accumulation on
681 the ashkabad fault (turkmenistan) from atmosphere-corrected insar, *J. Geophys. Res.*,
682 *118*(7), 3674–3690, doi:10.1002/jgrb.50236.

683 Webley, P. W., R. M. Bingley, A. H. Dodson, G. Wadge, S. J. Waugh, and I. N. James
684 (2002), Atmospheric water vapour correction to InSAR surface motion measurements
685 on mountains: results from a dense GPS network on Mount Etna, *Phys. Chem. Earth*,
686 *27*, 363–370, doi:10.1016/S1474-7065(02)00013-X.

687 Wen, Y., Z. Li, C. Xu, I. Ryder, and R. Bürgmann (2012), Postseismic motion after the
688 2001 M W7.8 Kokoxili earthquake in Tibet observed by InSAR time series, *J. Geophys.*
689 *Res.*, *117*(B8), B08,405, doi:10.1029/2011JB009043.

690 Wessel, P., and W. Smith (1995), New version of the Generic Mapping Tools released,
691 *Eos Trans. AGU*, *76*(329).

692 Williams, S., Y. Bock, and P. Fang (1998), Integrated satellite interferometry: Tropo-
693 spheric noise, GPS estimates and implications for interferometric synthetic aperture
694 radar products, *J. Geophys. Res.*, *103*(B11), 27,051–27,067, doi:10.1029/98JB02794.

Wright, T., B. Parsons, and E. Fielding (2001), Measurement of interseismic strain accumulation across the North Anatolian Fault by satellite radar interferometry, *Geophys. Res. Lett.*, *28*(10), 2117–2120, doi:10.1029/2000GL012850.

Wright, T. J., B. Parsons, P. C. England, and E. Fielding (2004), Insar observations of low slip rates on the major faults of western tibet, *Science*, *305*, 236–239, doi: 10.1126/science.1096388.

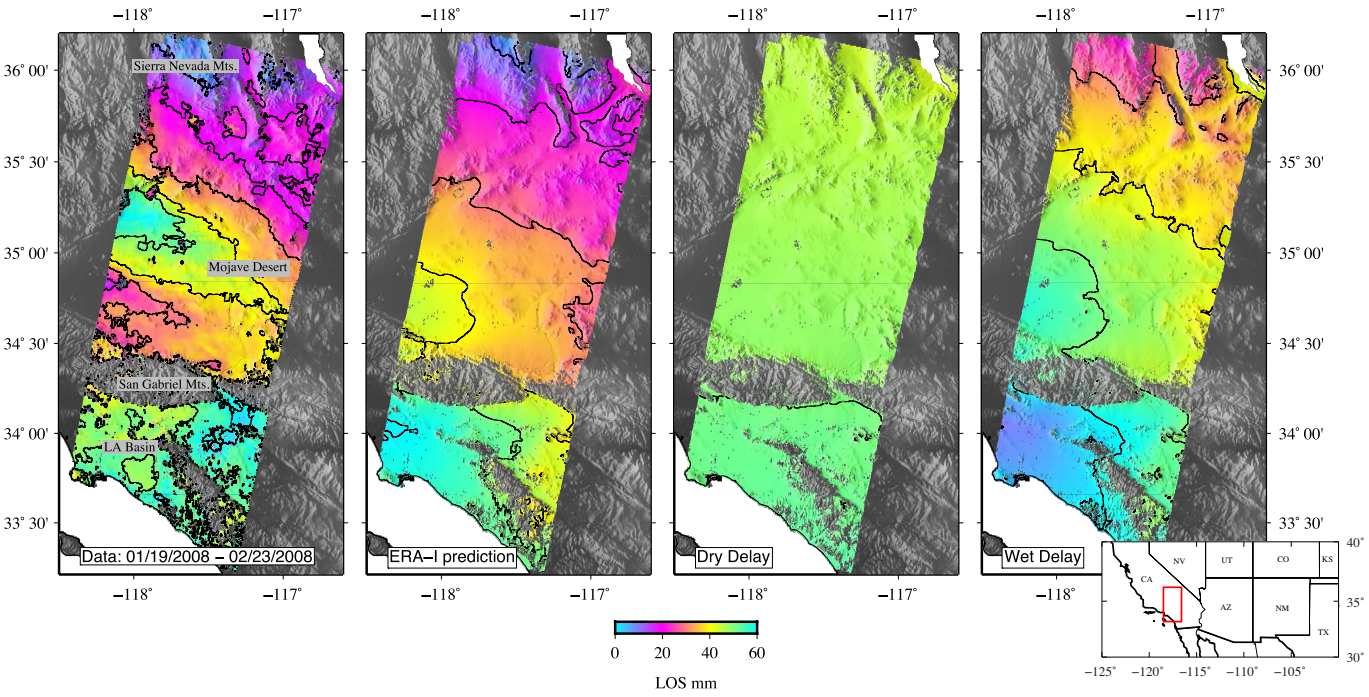

Figure 1. **Highlighting the effects of both delay components** - From Left to Right: An interferogram over southern California from Envisat SAR acquisitions on 01/19/2008 and 02/23/2008 on track 170, the corresponding stratified tropospheric delay predicted using ERA-Interim and the hydrostatic and wet components of the delay. One color cycle corresponds to 60 mm along the Line-Of-Sight (LOS) and 10 mm contour lines are plotted. Background shading is from SRTM DEM. To account for residual orbital errors, the original interferogram has been corrected from a linear trend in range and azimuth estimated on the residuals after correction from the ERA-Interim prediction.

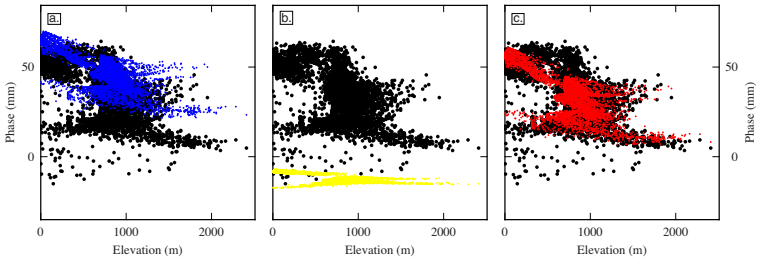

Figure 2. **Highlighting the effects of both delay components** - Phase/Elevation representation of the de-ramped interferogram shown in Fig. 1 (black dots), together with the wet component of the delay (a. blue dots), the hydrostatic component (b. yellow dots) and the total delay (c. red dots).

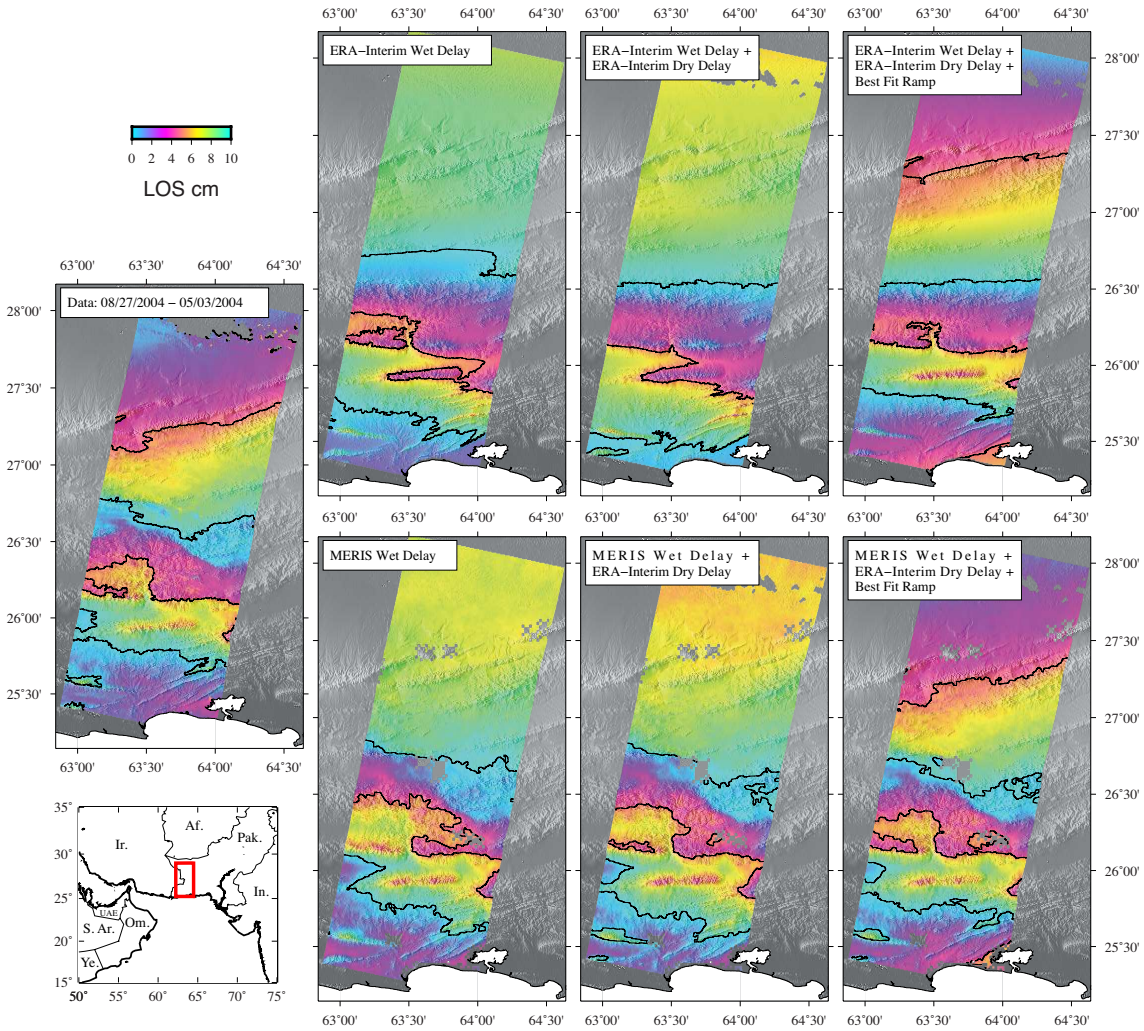

Figure 3. **Validation with MERIS** - Left: An interferogram over eastern Makran (Pakistan) from Envisat SAR acquisitions on 08/27/2004 and 05/03/2004 on track 449. Six panels to the right show the corresponding wet, total and total de-ramped tropospheric delay predictions using ERA-interim (Top) and MERIS (Bottom). One color cycle corresponds to 5 cm along the LOS direction and 10 cm contour lines are indicated. Background shading is from SRTM DEM.

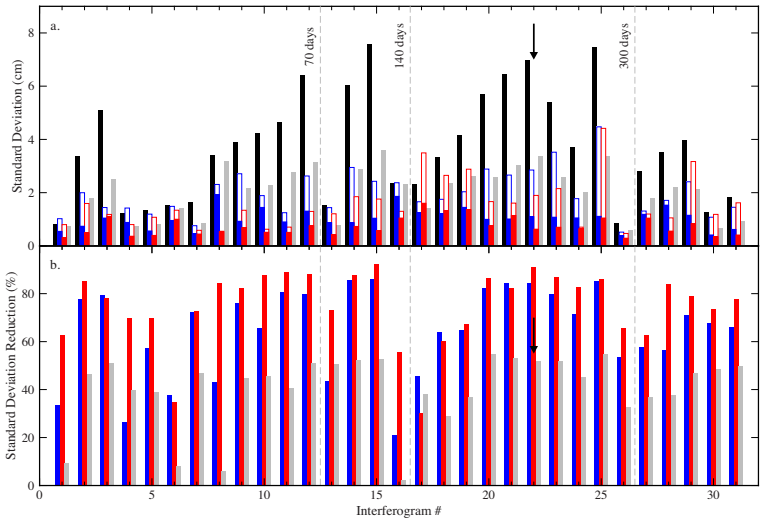

Figure 4. **Validation with MERIS** - a. Standard deviation of the original interferograms (black bars) compared to the residual standard deviation after correcting for the tropospheric delay derived from MERIS (red bars) and ERA-Interim (blue bars). Filled colored bars include removal of a 2-D best-fit linear function to account for potential orbit uncertainties, while white bars do not include such a correction. Gray bars are standard deviation of the original interferogram corrected with a 2-D best-fit linear function. b. Reduction of standard deviation after correction of the interferograms using MERIS (red bars) and ERA-Interim (blue bars), including a 2-D best-fit linear function. The x-axis is the interferogram number. Interferograms are ordered in terms of their respective timespan. Interferograms have been computed from ASAR Envisat acquisitions covering the eastern Makran (Pakistan), on track 449. Only interferograms corresponding to acquisitions with MERIS data with less than 30% cloud coverage are used. Arrow indicates the interferogram presented on figure 3. For examples of corrections, refer to Supp. Mat.

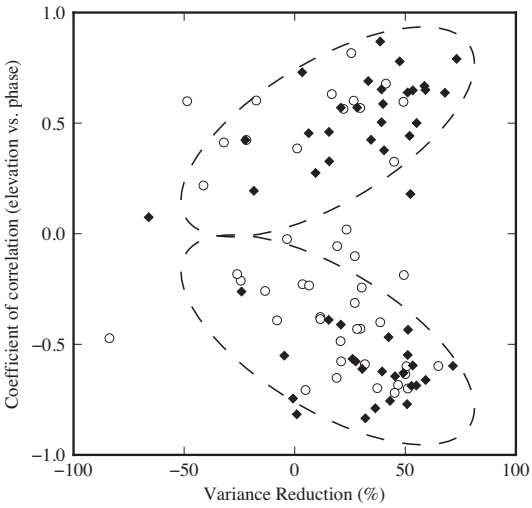

Figure 5. Influence of the turbulence on the quality of the prediction - Coefficient of correlation between interferometric phase and elevation as a function of the variance reduction when correcting a given interferogram with the ERA-I-derived delay. The interferograms used cover the Pakistani Makran area. Black dots are for interferogram on track 449. White dots are for interferograms on track 220. Maximum temporal baseline is 1 year to minimize the influence of possible tectonic deformation. Two symmetric ellipses encompass 90% of the points presented here. Positive percentage on the x-axis means the applied correction reduces the variance.

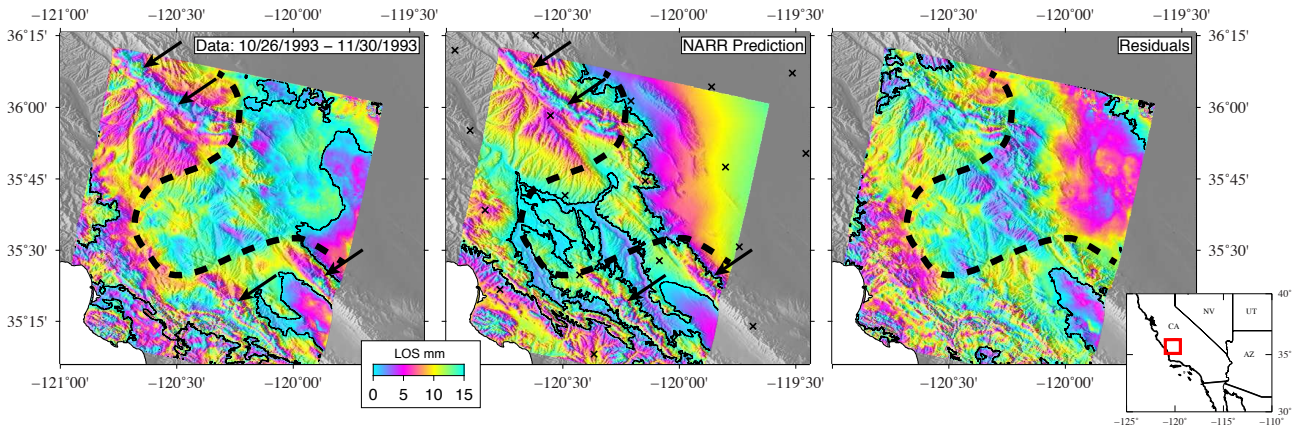

Figure 6. **Turbulent atmospheric delay** - Left: An interferogram centered over the Parkfield area, California, from ERS SAR acquisitions on 10/26/1993 and 11/30/1993. Center: Stratified tropospheric delay predicted using NARR. Black crosses indicate the position of NARR grid points. Right: Residuals after corrections of the data from the NARR prediction. One color cycle is 15 mm along the LOS direction and 15 mm contour lines are indicated. Background shading is from SRTM DEM. The thick dashed line indicates the position of an atmospheric front on the image. Black arrows indicate locations where the tropospheric stratification is visible.

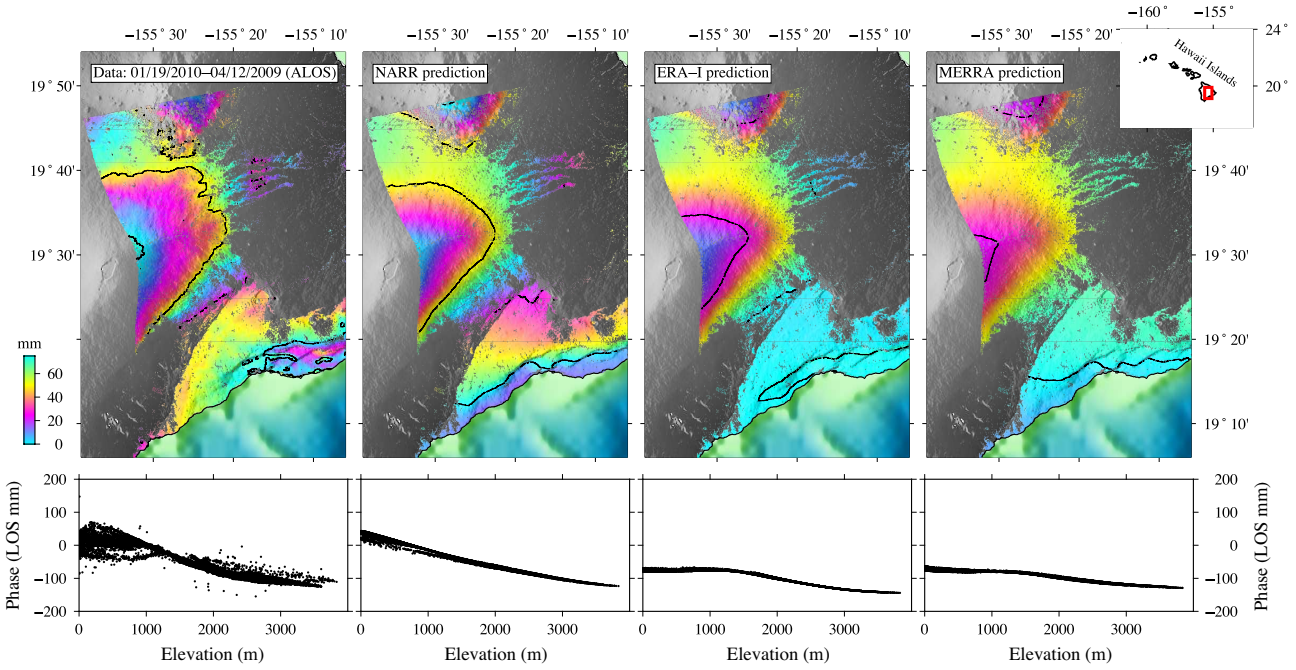

Figure 7. **Comparing predictions on Hawaii** - Interferogram over Kilauea volcano, Hawaii, from ALOS PALSAR acquisitions on 12/04/2009 and 01/19/2010 (top) and the corresponding Phase/Elevation plot (bottom), with the tropospheric delay derived from NARR, ERA-Interim and MERRA, and the associated predicted Phase/Elevation plots. These three different models show variable performances, as NARR seems to be the best match for this particular case. One color cycle corresponds to 75 mm along the Line-Of-Sight and 50 mm contour lines are indicated.

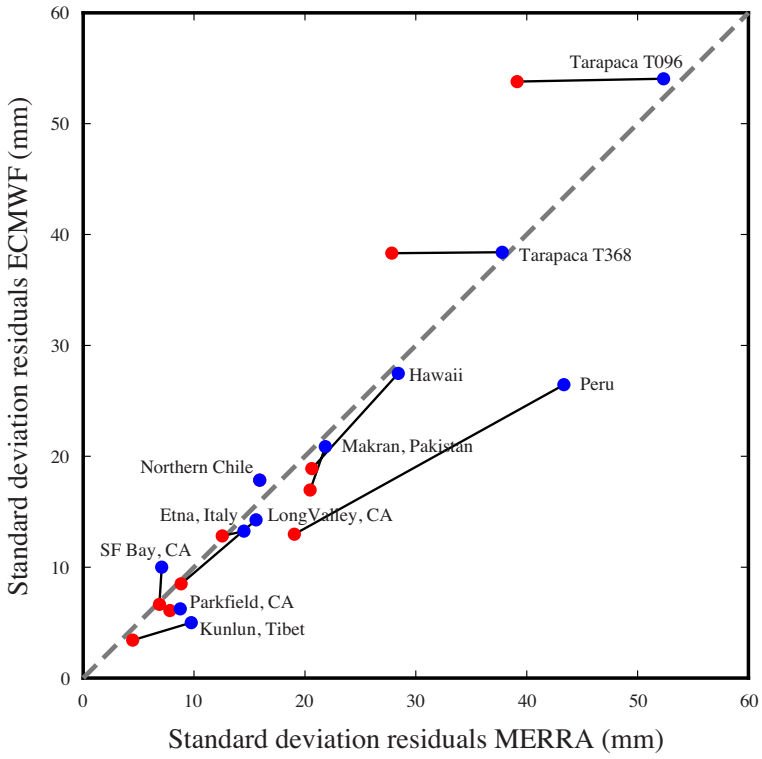

Figure 8. Comparison of the standard deviation of residuals after correction with ERA-Interim and MERRA predictions - Blue dots are the standard deviations of the residuals before removing a 2-D best-fit linear function to account for orbital uncertainties. Red dots are the standard deviation of the residuals after removing the 2-D best-fit linear function. The dashed gray line represents the one-to-one relationship.

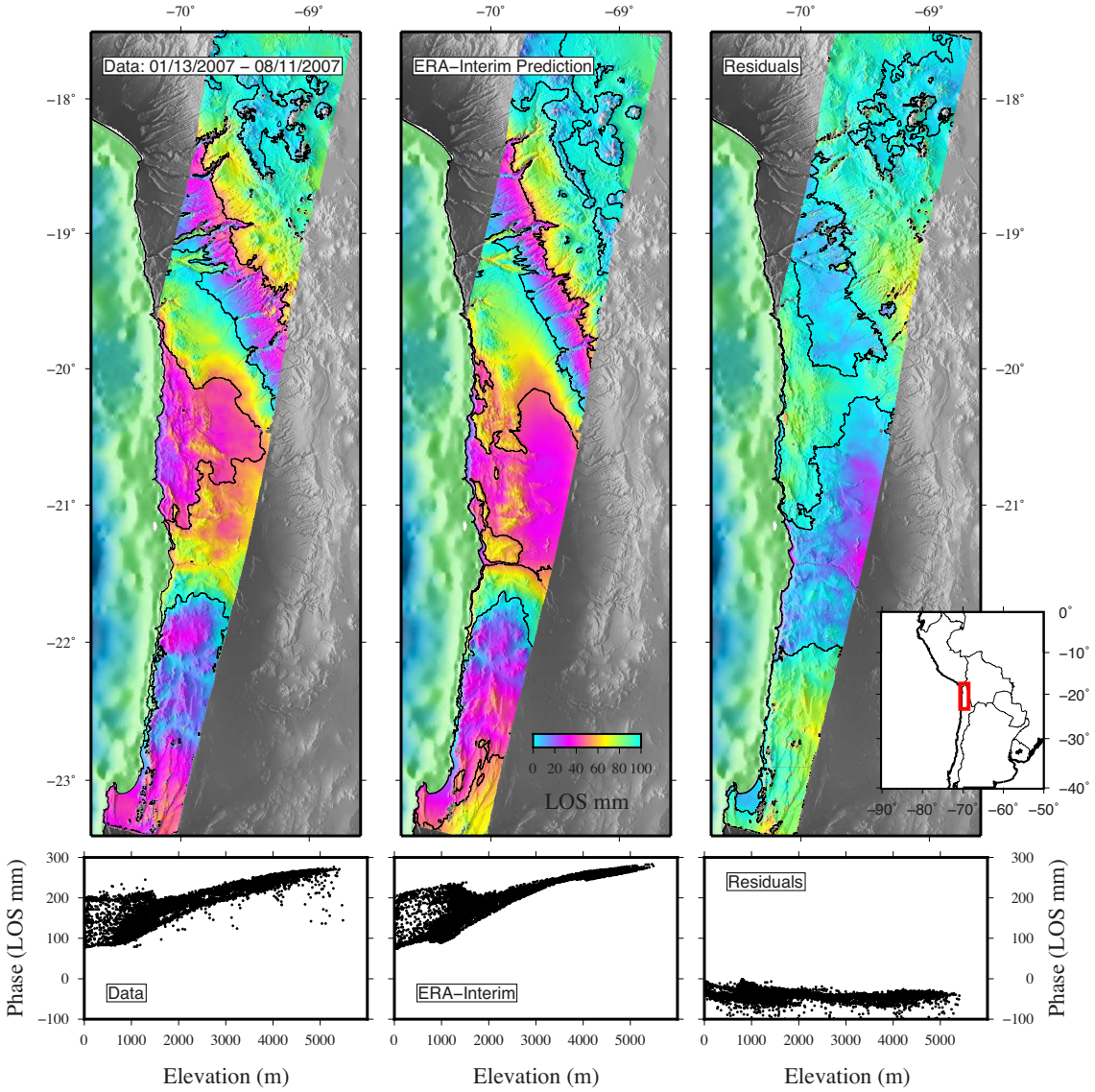

Figure 9. **Coastal setting** - Left: An interferogram over the north Chilean coast from Envisat SAR acquisitions on 01/13/2007 and 08/11/2007 (top) and the corresponding Phase/Elevation plot (bottom). Center: Stratified tropospheric delay predicted using ERA-Interim with the corresponding Phase/Elevation plot. Right: Residuals after correction with the ERA-Interim prediction. One color cycle corresponds to 100 mm along the Line-Of-Sight and 50 mm contour lines are indicated.

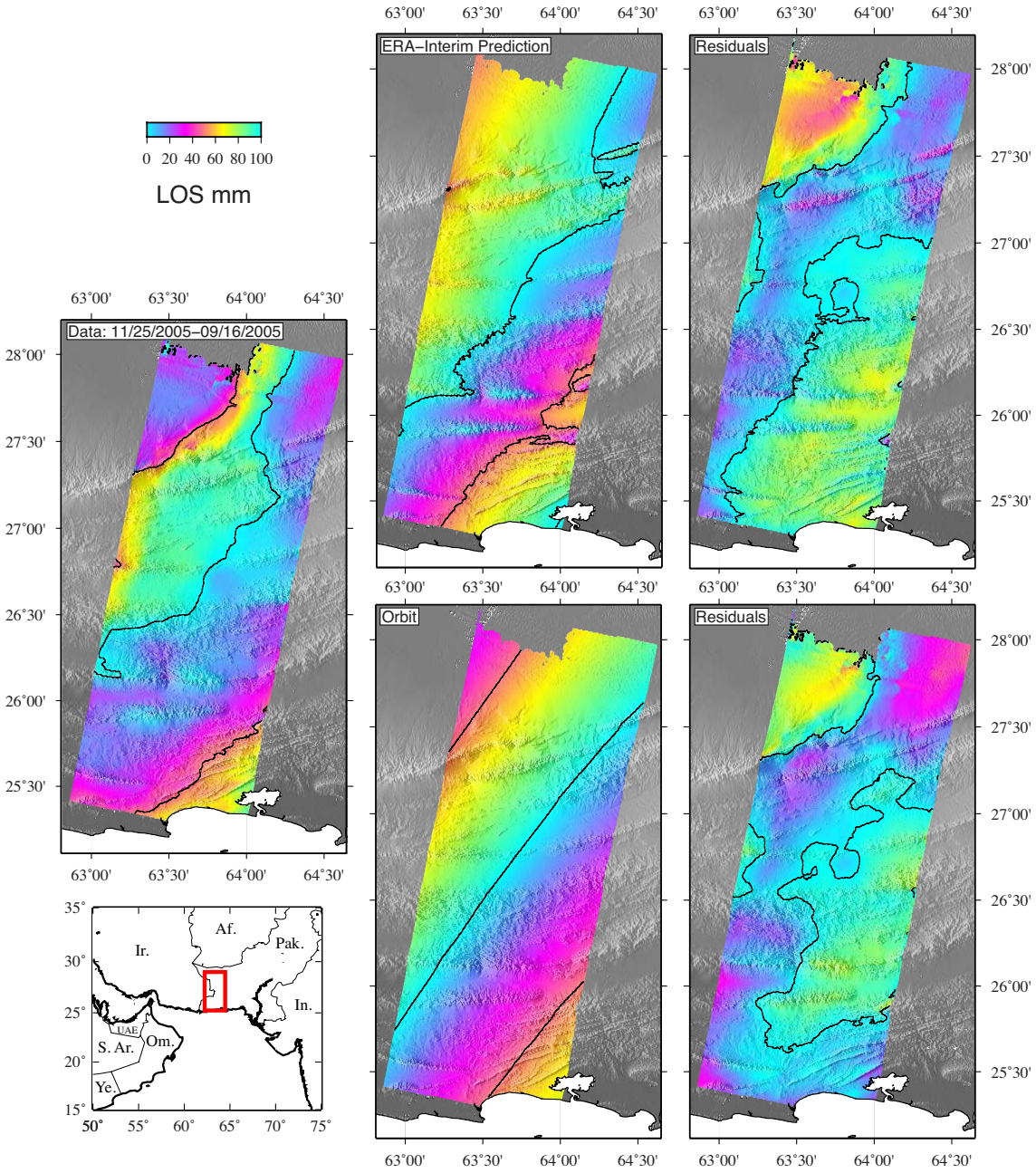

Figure 10. **Removing long wavelength signals with GAMs** - Left: Interferogram over the Makran region from Envisat SAR acquisitions on 09/16/2005 and 11/25/2005 on track 449. Top-Right: Stratified tropospheric delay predicted using ERA-Interim and corresponding residuals. Bottom-Right: Linear trend in range and azimuth, estimated on the interferogram and corresponding residuals. One color cycle corresponds to 100 mm and 50 mm contour lines are indicated.

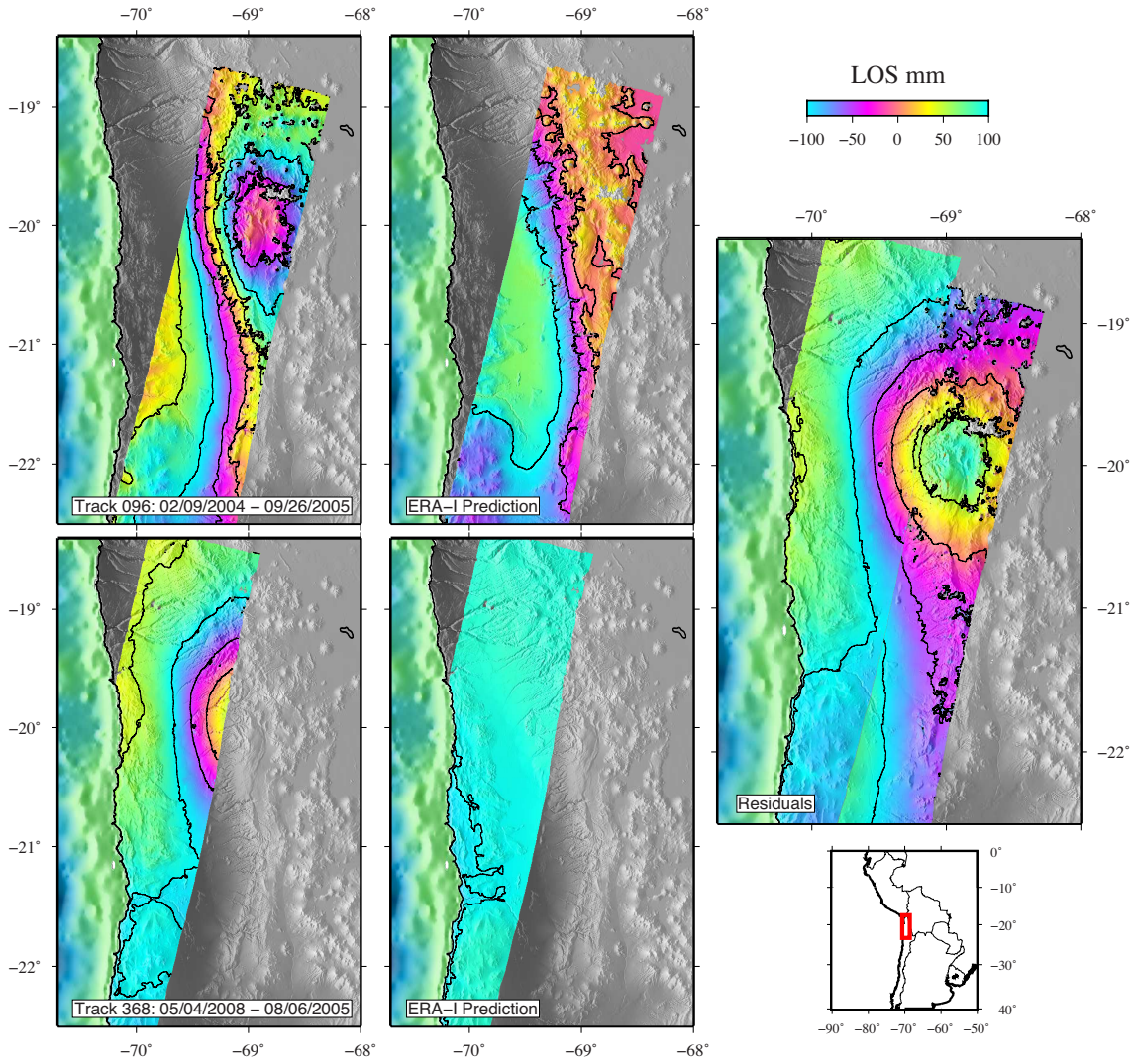

Figure 11. **The 2005 Mw 7.7 Tarapacá earthquake** - Left, Top and Bottom: Coseismic interferograms from Envisat SAR acquisitions on track 096 (Top, acquisitions on 02/09/2004 and 09/26/2005) and track 368 (Bottom, acquisitions 05/08/2004 and 08/06/2005). Center, Top and Bottom: Corresponding stratified tropospheric delay predicted using ERA-Interim. Right: Mosaic of the corrected interferograms. We note that no empirical linear trend has been removed and that both tracks overlap quite well. One color cycle corresponds to 200 mm and 50 mm contour lines are plotted. Background shading is from SRTM DEM.

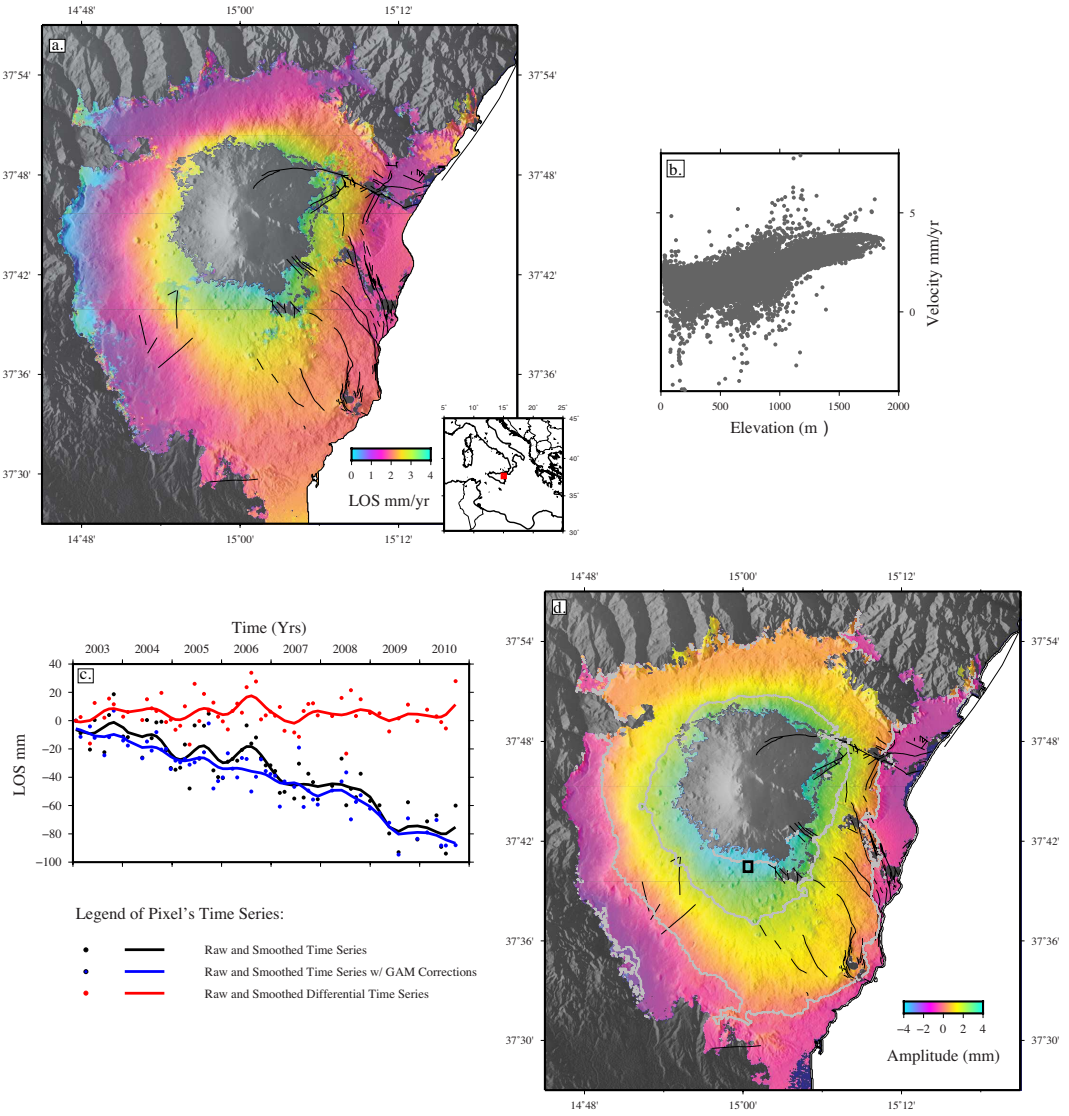

Figure 12. **Effect of tropospheric stratification on time series products - a.** Map of the difference between LOS displacement rates estimated using the NSBAS constrained inversion scheme with and without stratified tropospheric delay correction from ERA-I. One color cycle corresponds to 4 mm/yr. Major faults are indicated in black. Background shading is from SRTM DEM. We note that the velocity difference is strongly correlated with topography on the edifice. **b.** Phase velocity difference shown in a. as a function of pixels elevation. **c.** Pixel displacement between 2003 and 2010 from a time series with stratified tropospheric corrections derived from ERA-Interim, in blue, and without corrections, in black. The dots show the displacements. The lines show the displacement smoothed using a 75 days gaussian filter. Red dots and line show the difference. **d.** Map of the amplitude difference of a seasonal function fitted on time series estimated with and without stratified tropospheric corrections using ERA-Interim. Major faults are indicated in black. One color cycle corresponds to 8 mm and 2 mm contour lines are plotted. Background shading is from SRTM DEM. The black square indicates the location of pixel shown on a.